Fluorescent carbon nanodot-based rapid cell nucleus staining and application for diagnosis

Daiming Zhong [a], Huamin Yuan [a], Qiuyan Tian [a], Gongping Deng [b], Yanhong Ouyang [b], Yi Chen [c], Yang Wang [b], Zhiqin Yuan [d,*]

[a] Laboratory Medicine Department, Hunan Prevention and Treatment Institute for Occupational Diseases, Changsha 410000, Hunan, China
[b] Department of Emergency, Hainan General Hospital, Hainan Affiliated Hospital of Hainan Medical University, Haikou 570311, Hainan, China
[c] Hunan Zhixiangweilai Biotechnology Co., Ltd, Changsha 410125, Hunan, China
[d] College of Chemistry, Beijing University of Chemical Technology, Beijing 100029, China

Abstract

Cell nucleus status decides the activities of corresponding cells, making its rapid and effective staining important for revealing the actual condition of biological environment in life science and related fields. In this study, fast staining of cell nucleus is realized by fluorescent carbon nanodots (CDs). The staining mechanism is due to the positively charged CD surface-induced cell membrane penetration, which facilitates the CD-nucleus binding via electrostatic attraction. The size of cell nucleus is easily measured with fluorescence imaging technique. In addition, the CD-based cell nucleus stain is applied for discriminating the normal and cancer cells by determining the cell-to-nucleus ratio with fluorescence images.

Keywords: Cancer diagnosis, Carbon nanodots, Cell nucleus, Fluorescence imaging, Staining

1. Introduction

As the most important constituent part of cell, the nucleus shows key function on controlling cell growth and multiplication [1]. The contained genetic material largely coordinates with cell activities, including protein synthesis and cell division [2]. Thus, the status of cell nucleus can reflect the health condition, which has been applied for the diagnosis of diseases [3–6]. To achieve effective screening of cell nucleus, chemical stains with high staining efficiency have been explored [7–10]. For example, acridine orange has been applied for the cell nucleus staining with high brightness [11]. However, the high-cost of this probe and complicated operation restrict its wide application. In addition, some nuclear dyes that can interact with DNA have also been explored for cell nucleus staining [12,13]. For instance, DAPI is widely used for cell nucleus imaging due to its strong binding affinity toward DNA in nucleus [14]. Its blue emission and UV excitation, unfortunately, limits the usage in long-term imaging application. Therefore, the exploration of effective fluorescent stains for achieving rapid cell nucleus staining is appealing toward diagnosis application.

Recently, inorganic/organic fluorescent nanomaterials including metal nanoclusters, polymer dots and carbon nanodots (CDs), have attracted growing attention because of their high quantum yield and good biocompatibility [9,15–21]. For example, using polydopamine nanoparticles as the fluorescent probe, Ding et al. reported the in situ and label-free tracking of nucleus in long-term and real-time manners [9]. Among these fluorescent nanomaterials, CDs can be prepared from a variety of sources with low-cost and high biocompatibility attracts wide research interest in last two decades [22–31]. As an example, Liu et al. proposed a fluorescence method to reveal the RNA reduction using

Received 15 September 2023; accepted 18 March 2024.
Available online 15 June 2024

* Corresponding author.
E-mail address: yuanzq@mail.buct.edu.cn (Z. Yuan).

https://doi.org/10.38212/2224-6614.3503

CDs probe [32]. By combining CDs and gold nanoclusters (Au NCs), imaging of intracellular H_2O_2 has been achieved with CD-Au NC nanosatellite [33]. It has been reported that the rich surface functional groups of CDs endow effective cell penetration and strong interaction with organelle [34–37]. Additionally, the surface components can be easily regulated by changing the composition of raw materials. It is thus speculated that the CDs from proper raw materials might be a promising nuclear dye for cell nucleus staining.

According to the previous reports, materials with strongly positive charge show high affinity to negative cell organelle [38]. We thus hypothesize that CDs with positive charge could be used for achieving effective cell nucleus staining by electrostatic attraction, which is theoretically possible. In this study, we prepared CDs from *m*-phenylenediamine (MPD) and *o*-phenylenediamine (OPD) through electrolysis strategy, denoted as PD-CDs. The physical and optical properties have been studied with serial characterization techniques. Interestingly, the PD-CDs showed high cell nucleus staining efficiency, which was attributed to positive charge surface-mediated strong electrostatic attraction toward negative nucleus. With PD-CDs labeling, cell nucleus from normal and cancer cells can be easily differentiated, as illustrated in Fig. 1. The accuracy was also verified with the cell-to-nucleus ratio calculations. In a word, we proposed a simple and effective nuclear dye to realize rapid cell nucleus staining with PD-CDs.

2. Materials and methods

2.1. Chemicals and materials

Hydrochloric acid (HCl 36%), nitric acid (HNO_3), sulfuric acid (H_2SO_4), potassium chloride (KCl), sodium chloride (NaCl), magnesium chloride ($MgCl_2$), and manganese sulphate ($MnSO_4$) were purchased from Sinophorarm Chemical Reagent Corporation (Shanghai, China). Disodium hydrogen phosphate (Na_2HPO_4) and sodium dihydrogen phosphate (NaH_2PO_4) were purchased from J&K Scientific (Beijing, China). *m*-phenylenediamine (MPD) and *o*-phenylenediamine (OPD) was Adamas (Shanghai, China). Phosphate buffer saline (pH 7.4), DMEM cell culture media, carboxyfluorescein diacetate and DAPI were obtained from Hunan Zhixiangweilai Biotechnology (Changsha, China). All chemicals were used without further purification. HeLa cell and Oral epithelial cell were from Hunan Prevention and Treatment Institute for Occupational Diseases. Ultrapure water (18.2 MΩ) was obtained from a Millipore system. All glassware was cleaned by fresh aqua regia. Phosphate buffers were prepared according to a standard handbook. The pH values were measured with a benchtop pH meter (Orion plus, Thermo-Fisher, U.S.A.).

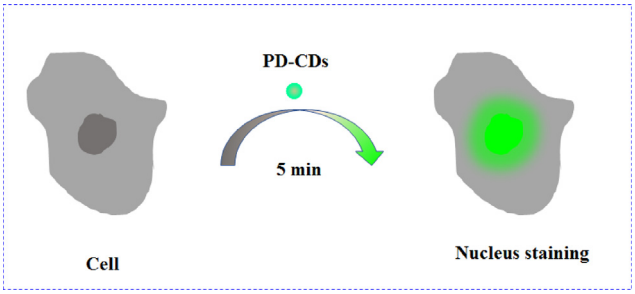

Fig. 1. Schematic illustration of cell nucleus staining with PD-CDs.

2.2. Apparatus

The UV–vis absorption spectra were collected using a UV–2450 spectrophotometer (Shimadzu, Japan). Fluorescence excitation and emission spectra were obtained with a F-7000 fluorescence spectrophotometer (Hitachi, Japan) at a slit of 5.0 nm with a scanning rate of 1200 nm/min. Zeta potential was determined using a Malvern Zetasizer 3000HS nano-granularity analyzer (Malvern, United Kingdom). The transmission electron microscopy (TEM) images were obtained using an HT7700 transmission electron microscope (Hitachi, Japan). The X-ray photoelectron spectroscopy (XPS) were recorded using an ESCALAB 250 X-ray photoelectron spectrometer with an Al Kα = 280.0 eV excitation source (Thermo, USA). The time-resolved fluorescence decay emission curve and fluorescence quantum yield measurements were performed on a FLS 980 fluorescence spectrophotometer (Edinburgh, UK). The absolute fluorescence QY was determined by using an integration sphere, the excitation and emission wavelengths were set at 438 nm and 515 nm. The fluorescence emission decay measurements were conducted with a 450 nm laser, and the lifetime was obtained through exponential decay fitting. The pH values were measured using a benchtop pH meter (Orion plus, Thermo Fisher, United States). The optical images of staining cells were acquired with a Ni–U multifunctional biomicroscope (Nikon, Japan).

2.3. Synthesis of PD-CDs

PD-CDs were synthesized with electrolysis method [39]. Typically, 0.01 g OPD and 0.01 g MPD were solubilized with 20 mL NaCl (0.1 M). After

complete dissolution, the electrolysis was conducted with a 10 V working potential. After turn on of the power, the solution color gradually changed from colorless to yellow with 20 min electrolysis, indicating the formation of PD-CDs. The formed PD-CDs were purified by dialysis bag (molecular retention Mw = 1000 Da) for 20 h to remove excess NaCl and unreacted OPD or MPD, and then was stored at room temperature before use.

2.4. Staining of cells

For conventional dye staining, HeLa cells were first cultured in DMEM medium at 37 °C, 5% CO_2 and saturated humidity [40]. After cells occupied the surface more than 70%, they were rinsed twice with 0.9% saline solution. Then, 0.5 mL of carboxyfluorescein/DAPI (10 μM) was added and the cells were stained for 30 min. After that, the cultured cells were washed with 0.9% saline solution twice. Finally, the fluorescence imaging was performed under a Nikon NI–U microscope with a FITC/DAPI filter and 100-w mercury lamp. For PD-CDs staining, the procedure is similar. Typically, HeLa cell and Oral epithelial cell were all cultured in DMEM medium at 37 °C, 5% CO_2 and saturated humidity [41]. After cells occupied the surface more than 70%, they were rinsed twice with 0.9% saline solution. Then, 1.0 mL of PD-CDs (100 mg/L) was added and the cells were stained for 5 min. After that, the cultured cells were washed with 0.9% saline solution twice to remove any excess PD-CDs. Finally, the fluorescence imaging was performed under a Nikon NI–U microscope with a FITC filter and 100-w mercury lamp. For the calculation of cell nucleus-to-cytoplasmic ratio (R), the cell area (Ac) was obtained by submit images to the Image J software. Then, the area of cell nucleus (An) was obtained based on the fluorescence intensity. Finally, the cell nucleus-to-cytoplasmic ratio was generated through an equation: R = An/(Ac-An).

3. Results and discussions

3.1. Synthesis and characterization of PD-CDs

At the beginning, electrolysis-mediated carbonization of OPD and MPD was used for synthesizing PD-CDs of 0.1 M NaCl diluted OPD and MPD solution at a voltage of 10 V. After 10 min electrolysis, the color of OPD and MPD mixture solution changed from colorless to yellow, indicating the formation of new species. At the same time, the solution showed bright green emission under 365 nm UV light irradiation, suggesting the generation of fluorescent species [27]. To reveal the newly generated species, the characterization of yellow solution with UV–vis absorption spectrometry, steady-state and time-resolved fluorescence spectrometry, FT-IR spectra, HRTEM, and XPS spectra were performed. As displayed in Fig. 2A, two peaks around 246 nm and 381 nm were observed. These characteristic absorption peaks can be assigned to the π-π* and n-π* electron transition [42]. Such a two absorption peaks profile usually appears in CD solution [39], indicating the possible production of fluorescent CDs. As shown in Fig. 2B, the fluorescence spectra of 1/10 diluted solution showed excitation and emission maxima at 438 nm and 515 nm. The large Stokes shift (78 nm) suggests the ignorable excitation influence during emission measurement. Notice that OPD-MPD mixture before electrolysis didn't show any visible emission. Thus, the bright green emission indicates the formation of PD-CDs. According to the TEM image (Fig. 2C), PD-CDs with spherical shape were observed. The average diameter was determined to be ~2.1 ± 0.2 nm from 100 counts. The crystal lattice of carbon, however, was not observed in HRTEM image. As shown in Fig. 2D, the Raman spectrum displayed a peak at 1562 cm^{-1} (G-band), representing sp^2 carbon in the system with in-plane vibration of C–C bonds. However, the peak at 1371 cm^{-1} (D-band) were not clearly observed.

The solution showed strong emission, the fluorescence quantum yield (QY) was measured by fluorescence spectrophotometer. The absolute QY of PD-CDs was determined to be 7.8%, suggesting its great potential in acting as imaging reporter or sensing probe. It is reported that the QY of inorganic materials is related to its electron transition process [43,44]. In some cases, long lifetime causes high QYs. The fluorescence lifetime character of PD-CDs was studied with time-resolved fluorescence emission spectra. As shown in Fig. 3A, a long fluorescence decay profile was observed. According to the fitting, the lifetime was calculated to be 10.6 ns, which is longer than many reported values of CDs [45]. It is reported that the surface state and surface functional groups are important to the fluorescence behavior of CDs, and the abundant C–O/C–N/C=N groups in high oxidation state may produces more of smaller energy gaps and induce diverse electron transition pathways [26]. To understand the surface composition, the FT-IR spectra of PD-CDs were obtained. As shown in Fig. 2E, the absorption peak around 1630 cm^{-1} was assigned to C=N bending vibration [46], while the absorption peak located at 1298 cm^{-1} was due to attributed to C–N bond vibration [47,48]. A visible absorption peaks around 928 cm^{-1} was

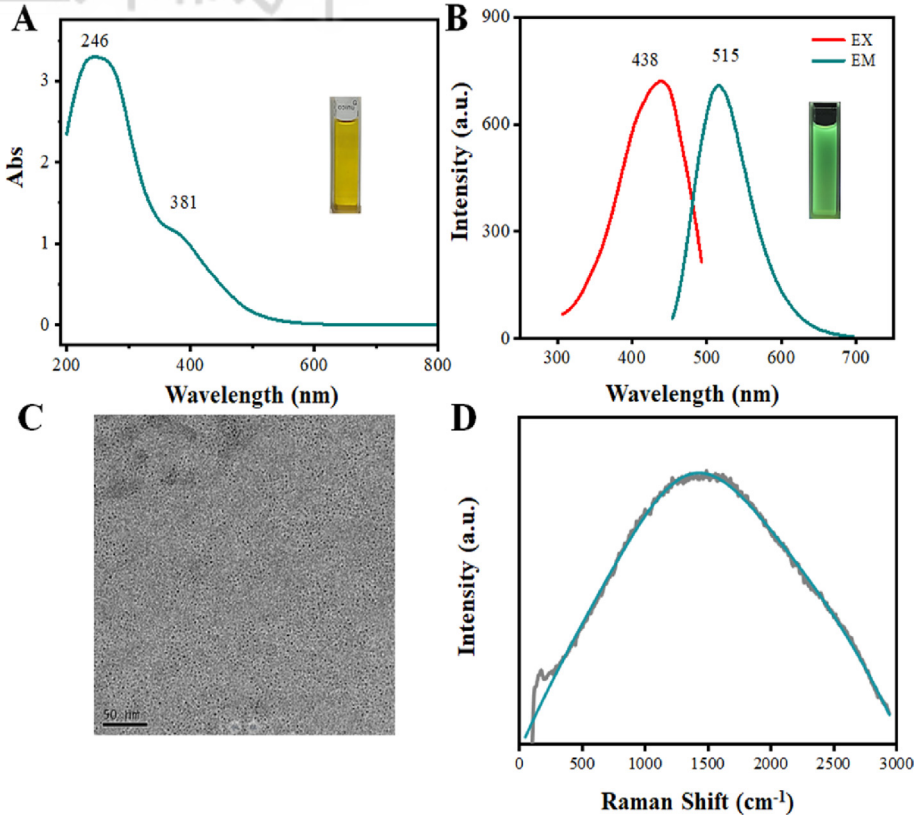

Fig. 2. (A) UV–vis absorption spectra of PD-CDs. Inset image was the corresponding solution under room light. (B) Fluorescence excitation (red line) and emission (blue line) spectra PD-CDs. Inset image was the corresponding solution under UV light illumination. TEM image (C) and Raman spectra (D) of PD-CDs.

observed, which belongs to N=N bending vibration [49–51]. In this work, the PD-CDs possess lots of nitrogen rich groups, leading to longer fluorescence lifetime. That means the azo compounds might form during the electrolysis treatment. The nitrogen-rich surface usually brings positive charge [52,53]. Based on the zeta potential results (Fig. 3C), the PD-CDs surface is positively charged (+11 mV).

To further study the element composition, the surface valence state of PD-CDs was characterized by XPS technique. As shown in Fig. 4A, the whole XPS spectrum of the PD-CDs was performed. The C 1s, N 1s, and O 1s signals were observed around 284, 400, and 532 eV, respectively. These sole element XPS spectra were analyzed through peak fitting treatment. Basically, the C 1s XPS spectrum (Fig. 4B) could be divided into two peaks (284.8 eV and 287.6 eV), meaning the existence of C–C and C–O/C–N bonds in PD-CDs [21]. Accordingly, the O 1s XPS spectrum (Fig. 4CD) was separated into three peaks (531.0 eV, 531.9 eV and 532.5 eV), which can be attributed to the C–O/N–O, C=O, and C–OH/C–O–C bonds, respectively. In addition, three peaks in the N 1s XPS spectrum (Fig. 4D) can be isolated, which locates at 398.9, 399.7, and 400.9 eV, respectively. These signals imply the existence of

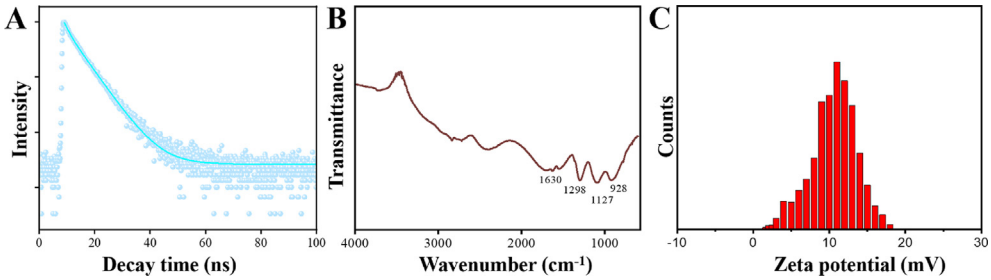

Fig. 3. Time-resolved fluorescence emission spectra (A), FT-IR spectra (B), and zeta potential results (C) of PD-CDs.

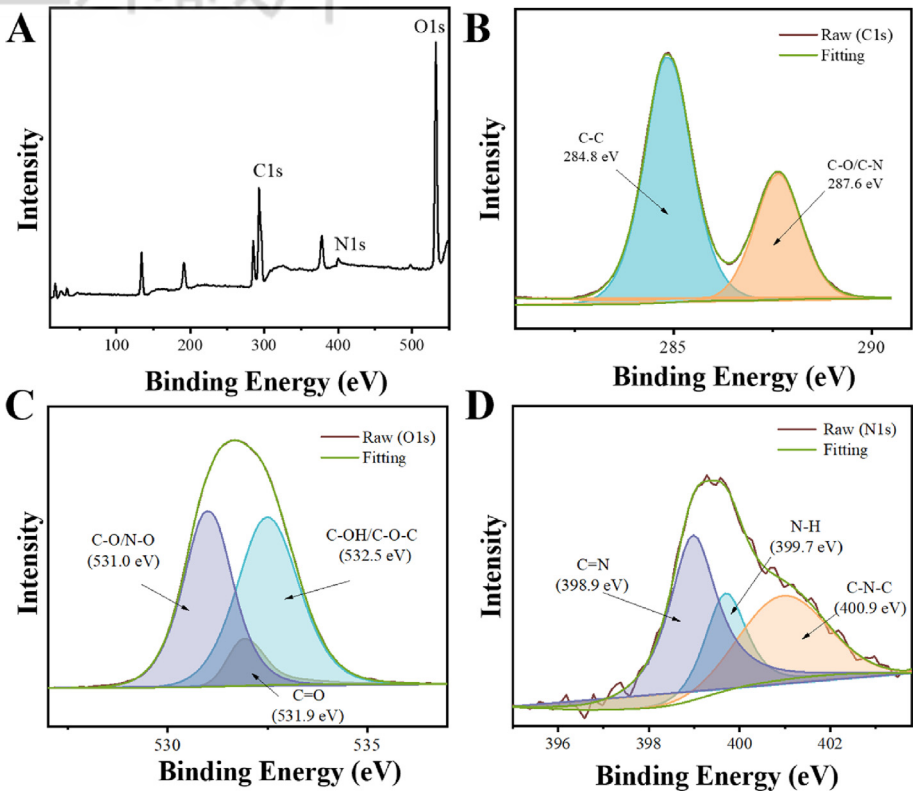

Fig. 4. (A) The full XPS spectra of PD-CDs. Individual C 1s (B), O 1s (C) and N 1s (D) XPS spectra of PD-CDs.

C=N/N=N, N−H, and C−N−C groups [48,50]. The XPS results reveal the nitrogen-rich surface composition, which decides the effective surface state and controls the fluorescence QYs. Taken together, the production of PD-CDs through the electrolysis of OPD-MPD solution was confirmed.

3.2. Cell staining with PD-CDs

Since the nucleus is important to cell function, fast staining greatly benefit the cell study and diagnosis. First, the staining of HeLa cell was conducted with conventional carboxyfluorescein diacetate and

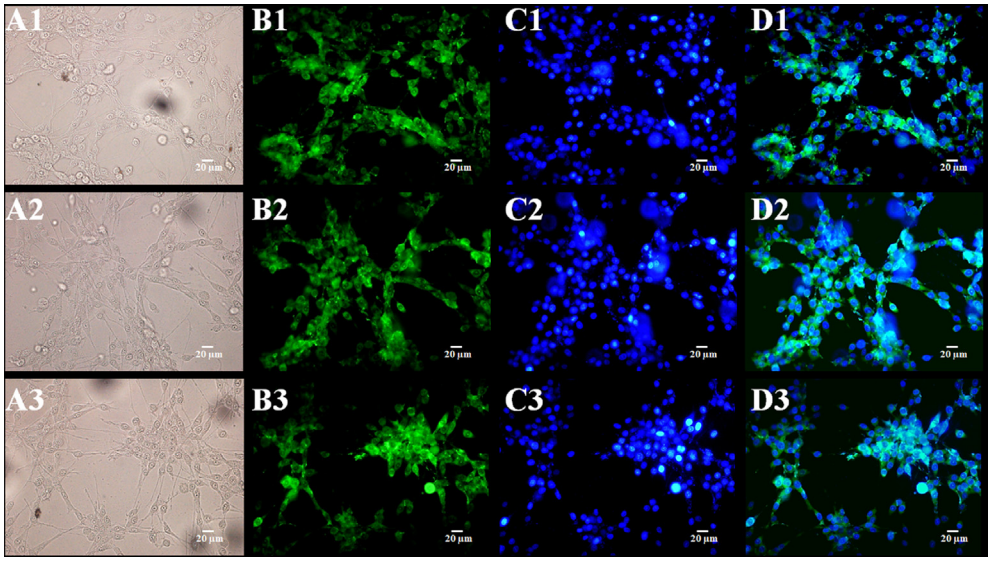

Fig. 5. Bright field (A), green fluorescence channel (B, carboxyfluorescein), blue fluorescence channel (C, DAPI), and merged (D) image of HeLa cell after incubation with conventional dyes with three repeats (1–3).

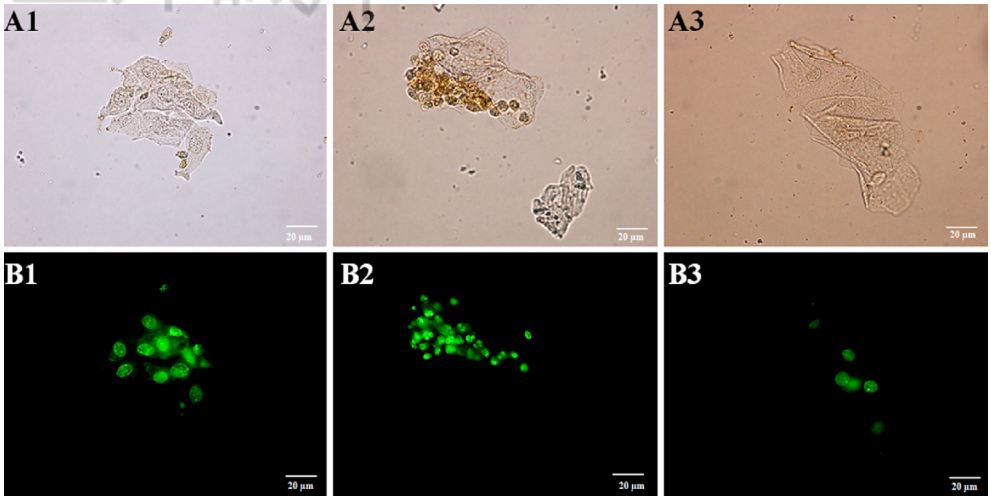

Fig. 6. Bright field (A) and fluorescence (B) image of HeLa cell after incubation with PD-CDs with three repeats (1–3).

DAPI. The carboxyfluorescein diacetate was used to label cytoplasm, while DAPI was widely used for nucleus imaging. As shown in Fig. 5, after 30 min staining, green emission from HeLa cell was observed, this is assigned to the carboxyfluorescein-labeled cytoplasm. The blue emission from DAPI-stained nucleus was also observed. According to the merge image, green emission and blue emission regions showed only slight overlap, indicating the successful staining of different cell region with designed dyes. The three repeated experiments showed similar results, indicting the accuracy of cell staining.

The high fluorescence QY and nitrogen rich surface characters suggest the potential in developing biological imaging probes with PD-CDs. The feasibility toward cell nucleus staining with PD-CDs was first investigated. In this work, two cell lines including HeLa cell and Oral epithelial cell were chosen. After 5 min incubation, fluorescence imaging of HeLa cell and Oral epithelial cell were conducted with an optical microscope. It was seen that the green emission from nucleus was observed in HeLa cell (Fig. 6). The dramatic green fluorescence indicates the successful stringing of cell nucleus with PD-CDs. In interestingly, the green fluorescence in Oral epithelial cell also proves the staining of normal cell (Fig. 7). The bright nucleus images demonstrate the potential application of cell nucleus staining with PD-CDs probe.

In order to verify the accuracy of cell nucleus staining with PD-CDs probe, the DAPI staining as control was conducted. It was seen that blue emission from DAPI and green emission from PD-CDs showed perfect overlap in cell nucleus region (Fig. 8). This suggested the practical application of

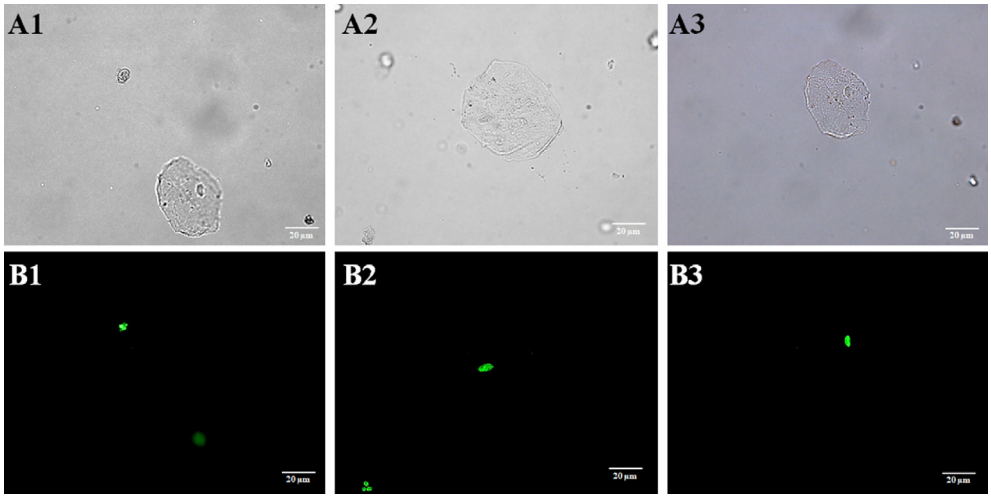

Fig. 7. Bright field (A) and fluorescence (B) image of Oral epithelial cell after incubation with PD-CDs with three repeats (1–3).

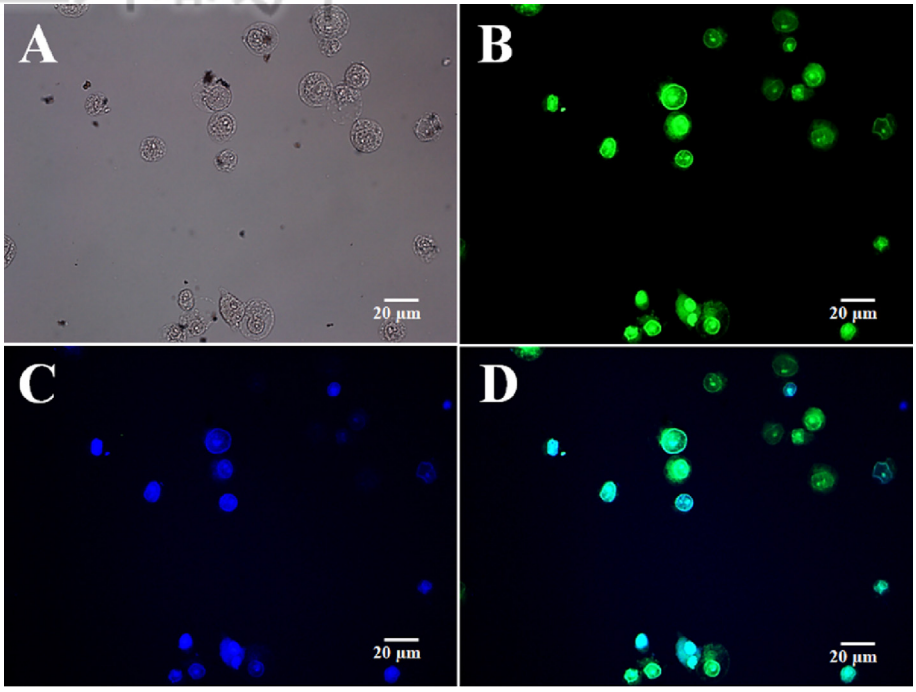

Fig. 8. Bright field (A), green fluorescence (B, PD-CDs), blue fluorescence (C, DAPI), and merged (D) image of HeLa cell after incubation with PD-CDs or DAPI.

PD-CDs as the potential cell nucleus staining agents. To illustrate the advantage of PD-CDs in comparison to commercial dye, the photostability testes of PD-CDs and DAPI dye were conducted under room light irradiation. As shown in Fig. 9, the relative fluorescence intensity of PD-CDs did not show dramatic decrease even after 7 days exposure. In contrast, the relative fluorescence intensity of DAPI dye showed distinct decrease in one day exposure. The diverse fluorescence intensity variations indicated the high photostability of PD-CDs.

The biocompatibility of PD-CDs was investigated. As shown Fig. 10, ignorable toxicity of PD-CDs appeared when the concentration was less than 300 mg/L. Therefore, the subsequent cell nucleus staining assays were conducted with 300 mg/L PD-CDs probe. The time-dependent of staining of nucleus by PD-CDs were obtained. Interestingly, the fluorescence from PD-CDs could be observed within 30 s, and the brightness maintained unchanged after 150 s incubations (Fig. 11). This indicated the rapid cell nucleus staining with PD-CDs. In this work, the PD-CDs were positively charged (+11 mV), which endows the strong binding affinity toward the DNA in cell nucleus. In comparison to partial existing nucleus staining agents, the proposed PD-CDs probe showed advantages of rapid staining character and high stability (Table 1).

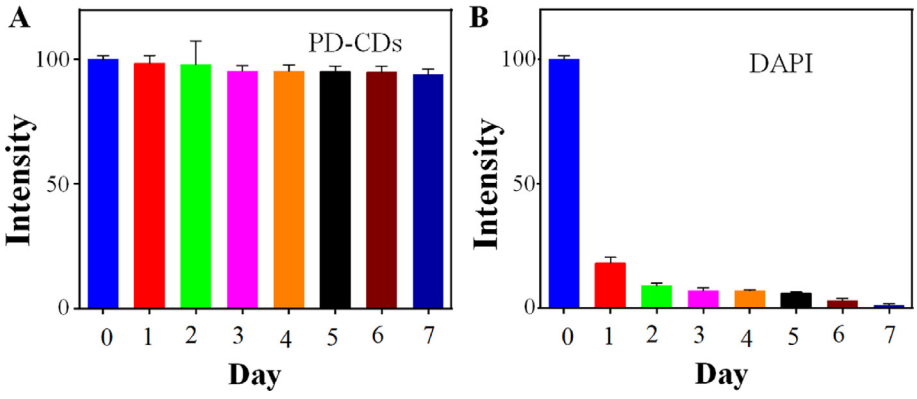

Fig. 9. Time-dependent relative fluorescence intensities of PD-CDs (A) and DAPI dye (B) under room light irradiation.

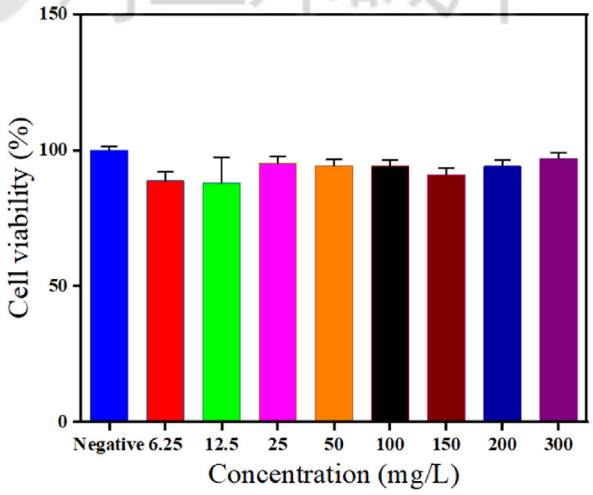

Fig. 10. The ckk-8 assay for PD-CDs in HeLa cells.

3.3. Application of cancer cell diagnosis

In clinical diagnosis, the cell nucleus-to-cytoplasmic ratio is an important parameter to evaluate the cell status. That is, large cell nucleus-to-cytoplasmic ratio usually represents unhealthy cell. And it is generally accepted that the cell nucleus-to-cytoplasmic ratio in cancer cells is larger than that of normal cells. Taken this into consideration, rapid differentiation of cancer cells and normal cells through cell-to-nucleus ratio is logic. In this case, normal cells possess high cell-to-nucleus ratio values, while cancer cells only show small cell-to-nucleus ratio values. According to Figs. 6 and 7, the staining area clearly show different size, which means the differentiation of HeLa cell and Oral epithelial cell through PD-CDs-based staining, is theoretical possible. Toward this goal, the cell images of HeLa cell and Oral epithelial cell under bright filed and fluorescence channels were obtained. As shown in Fig. 12, the size of staining cell nucleus in HeLa cell was much larger than that in Oral epithelial cell. The merged images distinctly showed that nucleus in HeLa cell almost fill the whole cell region. In contrast, nucleus in Oral epithelial cell only occupy small region. The cell-to-nucleus ratio was calculated by Image J software. Through the area measurements, the cell-to-nucleus ratio in HeLa cell was calculated to be 3.1 ± 0.3. In addition, the cell-to-nucleus ratio in Oral epithelial

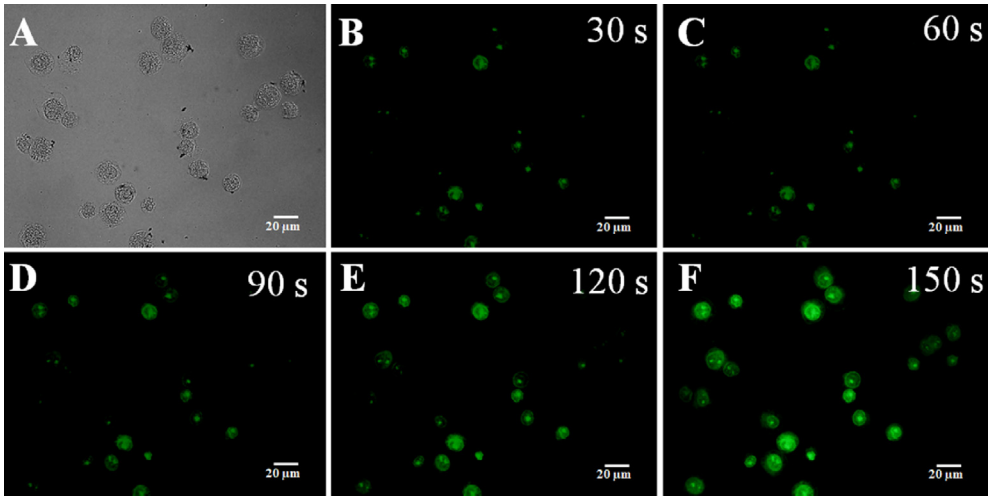

Fig. 11. Time-dependent fluorescence image of HeLa cells after incubation with PD-CDs.

Table 1. Comparison of the PD-CDs with some existing nucleus staining agents.

#	Materials	Ex/Em (nm)	Cell status	Incubation time (min)	specificity	Storage
1	Propidium iodide	535/617	Dead	5–60	DNA	−20 °C/No light
2	SYTOX-green	502/525	Dead	15–60	DNA/RNA	−20 °C/No light
3	Acridine orange	500/526	Live	15–60	DNA/RNA	−20 °C/No light
4	Ethidium bromide	510/600	Dead	15–20	DNA	−20 °C/No light
5	Hoechst33258	352/461	Live	15–60	DNA	−20 °C/No light
6	DAPI	358/462	Live	10	DNA	−20 °C/No light
7	PD-CDs	438/515	Live/Dead	2.5	DNA	No demand

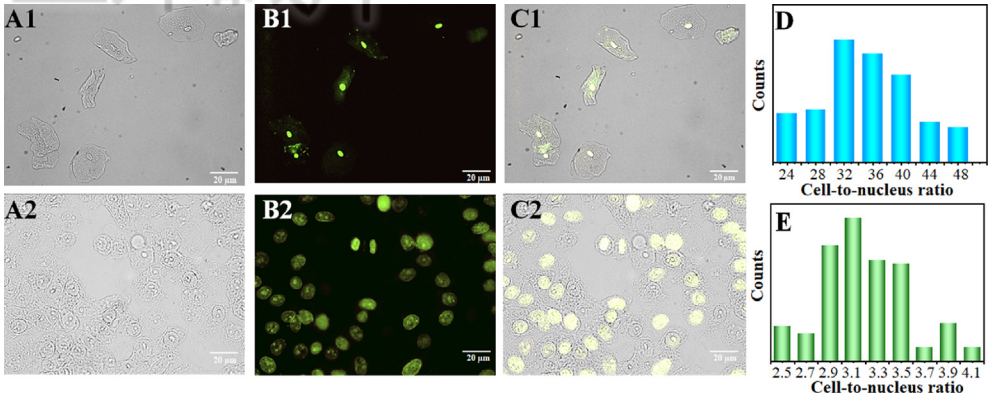

Fig. 12. Bright field (A), fluorescence (B) and merged (C) image of Oral epithelial cell (1) and HeLa cell (2) after incubation with PD-CDs (D) The statistical cell-to-nucleus ratio distribution of Oral epithelial cell (D) and HeLa cell (E), with 100 counts.

cell was calculated to be 34.4 ± 2.8. The dramatic difference supports the possible cell differentiation by PD-CDs-based cell nucleus staining. To simply differentiate the normal cells and cancer cells, the threshold of cell-to-nucleus ratio can be set as 10.0. That means, if the cell nucleus is less than 1/10 of the whole cell, it is healthy.

4. Conclusions

In summary, we have synthesized highly fluorescent and positively charged PD-CDs by electrolysis of OPD-MPD mixture for the rapid staining of cell nucleus. The positive surface is assigned for the rich nitrogen surface-mediated pronation, leading to effective cell penetration. Rapid cell nucleus staining with 5 min incubation is achieved based on PD-CDs labeling, which endows the visualization of cell nucleus by fluorescence imaging. With this PD-CDs probe, fast differentiation of Oral epithelial cell and HeLa cell is easily achieved through comparing the cell-to-nucleus ratio. Our work not only reports an effective nanoprobe to realize cell nucleus staining, but also provides a general tactic to discriminate normal cells and cancer cells based no cell-to-nucleus ratio. Thus, fast recognition of cancer cells through cell nucleus staining might be applied for clinical diagnosis.

Conflict of interest

The authors declare no competing financial interest.

Acknowledgment

This work was supported by the National Natural Science Foundation of China (22074005), the Natural Science Foundation of Beijing Municipality (2202038), Hainan Province Science and Technology Special Fund (ZDYF2020228, ZDYF2020125 and ZDYF2020114).

References

[1] Randall RS, Jourdain C, Nowicka A, Kaduchová K, Kubová M, Ayoub MA, et al. Image analysis workflows to reveal the spatial organization of cell nuclei and chromosomes. Nucleus 2022;13:279–301.
[2] Khatoon R, Jahan N, Khan HM, Rabbani T, Ahmad S. Evaluation of different staining techniques in the diagnosis of trichomonas vaginalis infection in females of reproductive age group. J Clin Diagn Res : JCDR 2014;8:DC05–8 [In eng].
[3] Xing F, Yang L. Robust nucleus/cell detection and segmentation in digital pathology and microscopy images: a comprehensive review. IEEE Rev Biomed Eng 2016;9:234–63.
[4] Van Gerwen OT, Smith SE, Muzny CA. Bacterial vaginosis in postmenopausal women. Curr Infect Dis Rep 2023;25:7–15.
[5] Chu L-A, Chang S-W, Tang W-C, Tseng Y-T, Chen P, Chen B-C. 5D superresolution imaging for a live cell nucleus. Curr Opin Genet Dev 2021;67:77–83.
[6] Feng Y, Zhang L, Yi Z. Breast cancer cell nuclei classification in histopathology images using deep neural networks. Int J Comput Assist Radiol Surg 2018;13:179–91.
[7] Venkatesh V, Shukla A, Sivakumar S, Verma S. Purine-stabilized green fluorescent gold nanoclusters for cell nuclei imaging applications. ACS Appl Mater Interfaces 2014;6:2185–91.
[8] Li M, Li Y, Xie R, Liu J, Gan L, Long M. Green synthesis of superior molecular fluorophores from chitosan assisted with cellulase for cell nucleus imaging and photosensitive printing. ACS Sustainable Chem Eng 2020;8:6323–32.
[9] Ding P, Wang H, Song B, Ji X, Su Y, He Y. In situ live-cell nucleus fluorescence labeling with bioinspired fluorescent probes. Anal Chem 2017;89:7861–8.
[10] Nakamura A, Takigawa K, Kurishita Y, Kuwata K, Ishida M, Shimoda Y, et al. Hoechst tagging: a modular strategy to design synthetic fluorescent probes for live-cell nucleus imaging. Chem Commun 2014;50:6149–52.
[11] Thomé MP, Filippi-Chiela EC, Villodre ES, Migliavaca CB, Onzi GR, Felipe KB, et al. Ratiometric analysis of Acridine Orange staining in the study of acidic organelles and autophagy. J Cell Sci 2016;129:4622–32.
[12] Sun W, Cui J-X, Ma L-L, Lu Z-L, Gong B, He L, et al. Imaging nucleus viscosity and G-quadruplex DNA in living cells using a nucleus-targeting two-photon fluorescent probe. Analyst 2018;143:5799–804.
[13] Zhang X, Ye Z, Zhang X, Man H, Huang Z, Li N, et al. A targetable fluorescent probe for dSTORM super-resolution

imaging of live cell nucleus DNA. Chem Commun 2019;55: 1951–4.
[14] Ghosh KK, Jeong Y-M, Kang N-Y, Lee J, Si Yan Diana W, Kim J-Y, et al. The development of a nucleus staining fluorescent probe for dynamic mitosis imaging in live cells. Chem Commun 2015;51:9336–8.
[15] Yang H, Lu F, Sun Y, Yuan Z, Lu C. Fluorescent gold nanocluster-based sensor array for nitrophenol isomer discrimination via an integration of host–guest interaction and inner filter effect. Anal Chem 2018;90:12846–53.
[16] Lu F, Yang H, Yuan Z, Nakanishi T, Lu C, He Y. Highly fluorescent polyethyleneimine protected Au_8 nanoclusters: one-pot synthesis and application in hemoglobin detection. Sensor Actuator B Chem 2019;291:170–6.
[17] Zhou J, Yang Y, Zhang C-y. Toward biocompatible semiconductor quantum dots: from biosynthesis and bioconjugation to biomedical application. Chem Rev 2015;115: 11669–717.
[18] Wang C-I, Wu W-C, Periasamy AP, Chang H-T. Electrochemical synthesis of photoluminescent carbon nanodots from glycine for highly sensitive detection of hemoglobin. Green Chem 2014;16:2509–14.
[19] Zhou D, Jing PT, Wang Y, Zhai YC, Li D, Xiong Y, et al. Carbon dots produced via space-confined vacuum heating: maintaining efficient luminescence in both dispersed and aggregated states. Nanoscale Horiz 2018;4:388–95.
[20] Xu D, Lin Q, Chang H-T. Recent advances and sensing applications of carbon dots. Small Methods 2020;4:1900387.
[21] Liang ZC, Kang MJ, Payne GF, Wang XH, Sun RC. Probing energy and electron transfer mechanisms in fluorescence quenching of biomass carbon quantum dots. ACS Appl Mater Interfaces 2016;8:17478–88.
[22] He H, Liu L, Chen X, Wang Q, Wang X, Nau WM, et al. Carbon dot blinking enables accurate molecular counting at nanoscale resolution. Anal Chem 2021;93:3968–75.
[23] Li RS, Liu JH, Yang T, Gao PF, Wang J, Liu H, et al. Carbon quantum dots–europium(III) energy transfer architecture embedded in electrospun nanofibrous membranes for fingerprint security and document counterspy. Anal Chem 2019;91:11185–91.
[24] Liu ML, Chen BB, Li CM, Huang CZ. Carbon dots: synthesis, formation mechanism, fluorescence origin and sensing applications. Green Chem 2019;21:449.
[25] Miao S, Liang K, Zhu J, Yang B, Zhao D, Kong B. Heteroatom-doped carbon dots: doping strategies, properties and applications. Nano Today 2020;33:100879.
[26] Liu Y, Zheng J, Liu W, Yuan Z, Lu C. Steady-state and dynamic bioanalysis using carbon quantum dot-based luminescence probes. ChemNanoMat 2022;8:e202200013.
[27] Yang HW, Lu FN, Zhan XX, Tian MC, Yuan ZQ, Lu C. A Eu^{3+}-inspired fluorescent carbon nanodot probe for the sensitive visualization of anthrax biomarker by integrating EDTA chelation. Talanta 2020;208:120368.
[28] Giordano MG, Seganti G, Bartoli M, Tagliaferro A. An overview on carbon quantum dots optical and chemical features. Molecules 2023;28:2772.
[29] Lin Z, Yu W, Hu R, Hu R, Wei Z, Zhang M. Dual-emission carbonized polymer dots combined with metal ions as a single-component fluorescence sensor array for pattern recognition of glycosaminoglycans. J Anal Test 2023;7: 285–94.
[30] Ye Q, Dai T, Shen J, Xu Q, Hu X, Shu Y. Incorporation of fluorescent carbon quantum dots into metal–organic frameworks with peroxidase-mimicking activity for high-performance ratiometric fluorescent biosensing. J Anal Test 2023;7:16–24.
[31] Chu HW, Unnikrishnan B, Anand A, Lin YW, Huang CC. Carbon quantum dots for the detection of antibiotics and pesticides. J Food Drug Anal 2020;28:539–57.
[32] Liu H, Geng X, Wang X, Wei L, Li Z, Lin S, et al. A carbonized fluorescent nucleolus probe discloses RNA reduction in the process of mitophagy. CCS Chem 2021;3: 3081–93.
[33] Li Z, Guo S, Yuan Z, Lu C. Carbon quantum dot-gold nanocluster nanosatellite for ratiometric fluorescence probe and imaging for hydrogen peroxide in living cells. Sensor Actuator B Chem 2017;241:821–7.
[34] Zhu SJ, Song YB, Zhao XH, Shao JR, Zhang JH, Yang B. The photoluminescence mechanism in carbon dots (graphene quantum dots, carbon nanodots, and polymer dots): current state and future perspective. Nano Res 2015;8:355–81.
[35] Cheng Y, Sun C, Ou X, Liu B, Lou X, Xia F. Dual-targeted peptide-conjugated multifunctional fluorescent probe with AIEgen for efficient nucleus-specific imaging and long-term tracing of cancer cells. Chem Sci 2017;8:4571–8.
[36] Gao D, Zhang Y, Zhu Y, Xin N, Wei D, Sun J, et al. Facile synthesis of dual-labeling carbon dots for simultaneous visualization of lipid droplets and lysosomes. Carbon 2023; 202:265–75.
[37] Mao Q-X, E S, Xia J-M, Song R-S, Shu Y, Chen X-W, et al. Hydrophobic carbon nanodots with rapid cell penetrability and tunable photoluminescence behavior for in vitro and in vivo imaging. Langmuir 2016;32:12221–9.
[38] Metwally S, Stachewicz U. Surface potential and charges impact on cell responses on biomaterials interfaces for medical applications. Mater Sci Eng C 2019;104:109883.
[39] Xiong Y, An Q, Qiao N, Chen Y, Zhou J-Q, Luo D-N, et al. Electrolysis-mediated rapid synthesis of highly fluorescent and pH responsive Congo red carbon nanodots for Cu2+ sensing. ChemistrySelect 2022;7:e202203435.
[40] Gao T, Wang S, Lv W, Liu M, Zeng H, Chen Z, et al. A self-assembled nanoprobe for long-term cancer cell nucleus-specific staining and two-photon breast cancer imaging. Chem Commun 2018;54:3578–81.
[41] Wu H, Pang L-F, Wei N, Guo X-F, Wang H. Nucleus-targeted N-doped carbon dots via DNA-binding for imaging of hypochlorous in cells and zebrafish. Sensor Actuator B Chem 2021;333:129626.
[42] Liu YQ, Seidi F, Deng C, Li RY, Xu TT, Xiao HN. Porphyrin derived dual-emissive carbon quantum dots: customizable synthesis and application for intracellular Cu2+ quantification. Sensor Actuator B Chem 2021;343:130072.
[43] Dimos K, Arcudi F, Kouloumpis A, Koutselas IB, Rudolf P, Gournis D, et al. Top-down and bottom-up approaches to transparent, flexible and luminescent nitrogen-doped carbon nanodot-clay hybrid films. Nanoscale 2017;9:10256–62.
[44] Yuan Z, Cai N, Du Y, He Y, Yeung ES. Sensitive and selective detection of copper ions with highly stable polyethyleneimine-protected silver nanoclusters. Anal Chem 2014;86:419–26.
[45] Sun Y, Lu F, Yang H, Ding C, Yuan Z, Lu C. Fluorescent sensor array for separation-free dopamine analogue discrimination via polyethyleneimine-mediated self-polymerization reaction. Nanoscale 2019;11:12889–97.
[46] Zhou H, Yang Q, Lu F, Zheng J, Yuan Z, Lu C. Fluorescence-based self-diagnosis of hyperbranched polyethyleneimine oxidation. Talanta Open 2024;9:100284.
[47] Zhu PP, Li JY, Gao LX, Xiong J, Tan KJ. Strategy to synthesize tunable multiemission carbon dots and their multicolor visualization application. ACS Appl Mater Interfaces 2021;13: 33354–62.
[48] Chandra S, Kundu T, Kandambeth S, BabaRao R, Marathe Y, Kunjir SM, et al. Phosphoric acid loaded azo (–N═N–) based covalent organic framework for proton conduction. J Am Chem Soc 2014;136:6570–3.
[49] Liu S, Xu X, Kang Y, Xiao Y, Liu H. Degradation and detoxification of azo dyes with recombinant ligninolytic enzymes from Aspergillus sp. with secretory overexpression in Pichia pastoris. R Soc Open Sci 2020;7:200688.
[50] Zhou Z-B, Tian P-J, Yao J, Lu Y, Qi Q-Y, Zhao X. Toward azo-linked covalent organic frameworks by developing linkage chemistry via linker exchange. Nat Commun 2022;13:2180.
[51] Li Z, Wang L, Tian M, Li Z, Yuan Z, Lu C. Tris–Co(II)–H_2O_2 system-mediated durative hydroxyl radical generation for efficient anionic azo dye degradation by integrating electrostatic attraction. ACS Omega 2019;4:21704–11.

[52] Ghezzi F, Donnini R, Sansonetti A, Giovanella U, La Ferla B, Vercelli B. Nitrogen-Doped carbon quantum dots for biosensing applications: the effect of the thermal treatments on electrochemical and optical properties. Molecules 2023;28:72.

[53] Zhou H, Zhang J, Liu Y, Liu W, Tang Y, Yuan Z, et al. Polyamine-assisted rapid gold nanocluster synthesis via electrostatic attraction-facilitated core approaching. ChemistrySelect 2022;7:e202103347.